Research Article

Research on the prediction method of unbalance responses of dual-rotor system based on surrogate models

Xu Chen[1] · Hao Zhang[2] · Cunjian Zou[1] · Jingyu Zhai[1] · Qingkai Han[1]

Received: 26 July 2019 / Accepted: 28 November 2019 / Published online: 3 December 2019
© Springer Nature Switzerland AG 2019

Abstract
In this work, the prediction methods of unbalance responses based on the surrogate models were studied, where the simulation data of vibration responses of a dual-rotor system with four disks and five supportings were involved. Firstly, based on the Latin hypercube sampling and random sampling with uniform distribution of unbalance distribution of the fan disc and the hyper-compressor disc, the input variables of the training samples and the testing samples were respectively obtained. According to the sampling results, the multi-body dynamics simulations were conducted to extract the vibration responses at the corresponding measuring points as the output variables of the sample space. Then, the algorithms of multivariate adaptive regression splines (MARS), radial basis function (RBF) and Kriging, were selected to respectively construct the response-predicted models of the rotor system. Finally, predicted vibration responses were figured out by surrogate models and the prediction accuracies were verified by comparison with output parameters in the testing samples. The results showed that the prediction methods of unbalance responses based on MARS, RBF and Kriging enjoyed high prediction accuracies according to the standards, which were proved to be feasible in theoretically.

Keywords Dual-rotor system · Surrogate model · Latin hypercube sampling · Dynamic simulation · Accuracy test

1 Introduction

In the application and development of aero-engine, unbalance force caused by unbalance mass in the multiple discs of the low-pressure fan section and the high-pressure compressor section will cause serious vibration, which is one of the most major vibration sources of aero-engine. However, the research on the unbalanced vibration response characteristics of aero-engine often faces the following problems and challenges. Firstly, complex structure and narrow internal space of the dual-rotor system make it difficult to place sensor. Secondly, it is the commonly used method in the field of engineering practice that obtaining a reliable response values in steady state of the system running through multiple start-stops, which costs a lot in time and economy.

At present, the researches of rotor unbalance are mainly the exploration of vibration characteristics. AL-Shudeifat et al. [1] numerically and experimentally found the change in the unbalance force angle with respect to the crack opening direction significantly altered the values of the critical whirl speeds and their corresponding peak whirl amplitudes in cracked rotor-bearing-disk systems for starting up operations. The research of Gao, P.'s revealed that the increasement of corresponding critical speeds and the vibration amplitudes of rotors happened, as the unbalances in LP and HP rotors mainly increased in a force model for the inter-shaft bearing with a local defect on the surface of the outer race or the inner race [2]. Cao et al. [3] analyzed quantitatively the effect of angular speed fluctuation on vibration responses of the unbalanced rotor, the result of which showed the speed fluctuation produced

✉ Qingkai Han, qk.han@hotmail.com | [1]School of Mechanical Engineering, Dalian University of Technology, Dalian 116023, China. [2]College of Mechanical Engineering and Automation, Liaoning University of Technology, Jinzhou 121001, China.

apparent frequency modulation, phase distortion and amplitude error of the unbalance. The research of Ref. [4] showed the sensitive intervals of unbalance vibration in the input side and output side are respectively in lower frequency and in higher frequency in a gas turbine rotor system. Zhang [5] proposed a non-whole beat correlation method to identify the unbalance responses, which was proved to be feasible and practicable from the numerical simulation and balancing experiment.

It is a fitting technology for the surrogate model that predicts the response value in the unknown situation using those in the known situation. Its essence is to approximately express the relationship between the input and output data through establishing the mapping between them, taking the fitting precision and the prediction precision as the constraints. With the application and development of surrogate model technology for more than 40 years, it has been quite mature in the applications of optimization design [6–12] and parameter identification [13–15] of complex engineering problems, replacing the high-precision model with heavy computation and solving the problem that analytical model cannot be established in some engineering fields. The introduction of surrogate model technology in the dual-rotor system, can establish the model vibration response of by the use of limited sample data to efficiently achieve accurate prediction for the unknown.

In the field of rotor dynamics, some progress in the application of surrogate model technology has been made. The research of the Ref. [16] illustrated the effectiveness of Kriging when predicting the critical speeds and the vibration amplitudes of a single flexible rotor modelled by analytic method. The research of the Ref. [17] used a polynomial surrogate method to effectively analysis steady-state response of cracked rotors with uncertain-but-bounded parameters by numerical simulations. Gu et al. [18] realized the identification of single-point unbalance parameters of the single-rotor system model, based on the PSO-SVR model, but there are not results for the multi-point and the dual-rotor. The research of the Ref. [19] presented a new method based on an improved Kriging surrogate model and evolutionary algorithm (IKSMEA), which was proved to effectively and accurately identify the structure parameters of a nonlinear rotor-bearing system by numerical studies and experimental validation.

In this study, multi-measuring-point metamodellings of a typical dual-rotor system with double unbalance disks were established based on MARS, RBF and Kriging in sequence, and successfully predicted the vibration amplitudes under the unknown working conditions which were randomly sampled with uniform distribution, proving the application feasibility in this field. The researches applying the metamodelling methods for predicting the vibration response of the dual-rotor system are quite few, so this paper is a supplement. This is an exploratory practice of applying the relatively mature mathematical technology to the engineering field, which can provide the reference for the dynamics balance and design of dual-rotor aero-engine.

2 Object, approach and algorithms

2.1 Object

Figures 1 and 2 show the rotor structure of a certain type of aero-engine, in which the numbers, 1–6, represent six bearing supports in the whole rotor system. Based on the principles of the structural similarity (1:2 reduced scale and similar characteristics of mass and moment of inertia) and dynamic similarity (the characteristics of first three order modes and Campbell diagrams of the high-pressure rotor, low-pressure rotor and the dual-rotor system are consistent with those of the prototype), a scaled model is obtained, as shown in Fig. 3. It is mainly composed of four parts, low-pressure fan disc (LPC), low-pressure turbine disc (LPT), high-pressure compressor disc (HPC) and high-pressure turbine disc (HPT). In Fig. 3, there are five supportings, among which bearings 1#, 2# and 5# support the LP rotor, and bearings 3# and 4# support the HP rotor; there are nine measuring points deployed in the rotors, with the purpose of monitoring the vibration responses. The measuring points 1, 2, 3, 4 and 5 are at the LP part, among which, measuring point 1 is the center of supporting 1#, measuring point 2 is the center of mass of the LPC, measuring point 3 is the center of supporting 2#, measuring point 4 is the center of mass of LPT, and measuring point 5 is the center of supporting 5#. The measuring points 6, 7, 8 and 9 are at the HP part, among which, measuring point 6 is the center of supporting 3#, measuring point 7 is the center of mass of the HPC, measuring point 8 is the center of

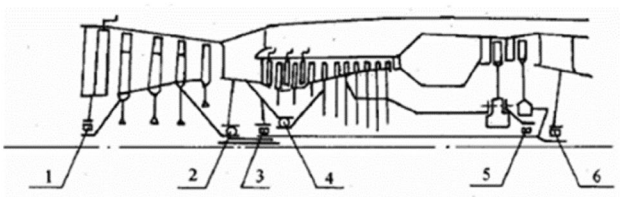

Fig. 1 The simplified model of a dual-rotor system

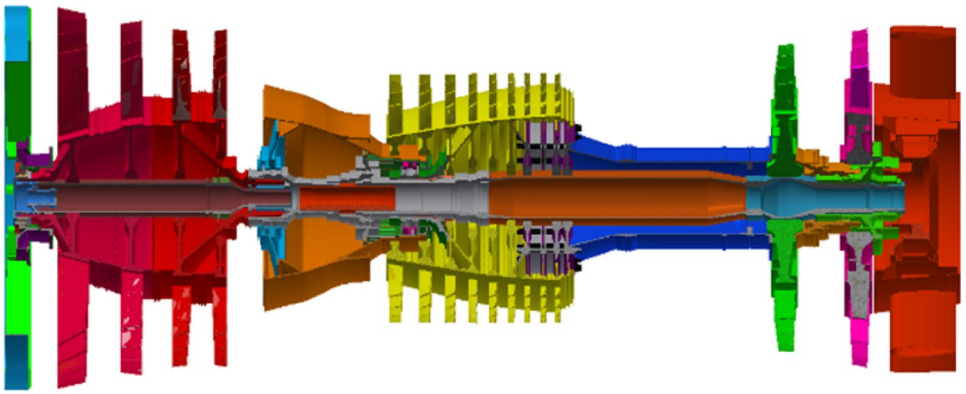

Fig. 2 3D solid model of the dual-rotor system

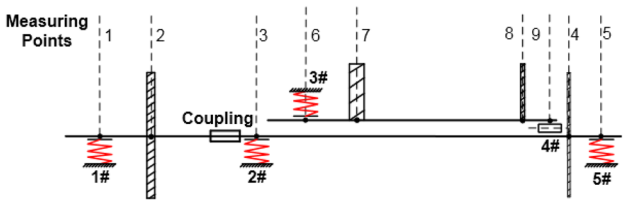

Fig. 3 The simplified model of a dual-rotor system

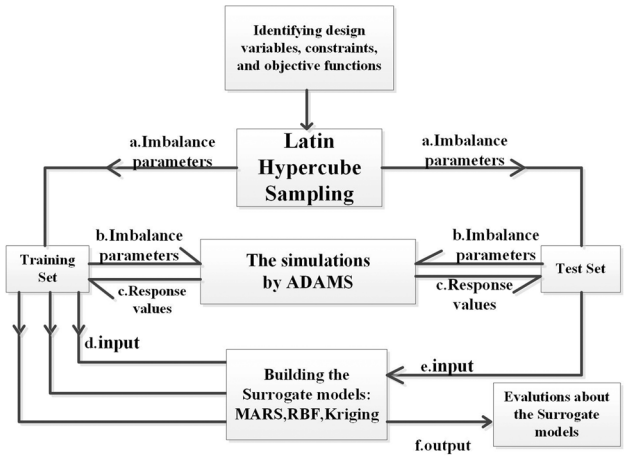

Fig. 4 Schematic diagram of predictions

mass of the HPT, and measuring point 9 is the center of supporting 4#.

2.2 Approach

The achievement of prediction process includes the following three steps: (1) selecting samples and sample quantity in the variable space by the experimental design method; (2) calculating the output response variables of each sample for the research object, and then, establishing the metamodellings by training points; (3) doing the prediction research and verifying the prediction accuracy of the results by testing points. The analysis process is shown in Fig. 4, in which letters, a to f, represent the orders of parameters inputted or outputted.

Design of experiment (DOE) is a scientific method to research the correlation between multiple factors and response variables [20]. Common DOE methods include Full Factorials Design, Orthogonal Experiment Design, Latin.

Hypercube Experiment Design, etc. Latin Hypercube Experimental Design is a random sampling method with the feature "space filling", which can ensure that the entire variable space is covered by sample points, so adopted to determine mass and phase of unbalance disks of training sets in the paper. It can be taken as the principle that the number of training points is 10 times that of design variables [21]. There are four variables in the variable space: unbalance mass and phase of the LPC and HPC, so forty is the number of training samples. In order to verify the accuracy of the established models, the eleven testing points are randomly sampled with uniform distribution in the variable space. The distributions of training points and testing points are shown in Figs. 5 and 6.

Then, unbalance parameters are set so that the dynamic simulations in ADAMS are carried out to obtain the vibration responses of multiple measuring-points under 51 working conditions. ADAMS software is the most excellent dynamic simulation software of mechanical system developed by MDI. It is one of the most authoritative and widely used dynamic analysis software of mechanical system in the world. It applies Lagrange method to calculate multi-body dynamics, which is a relative coordinate method. The form of its dynamic equation is the second order differential equations of Lagrange coordinate matrix, namely $A(q,t)\ddot{q} = B(q,\dot{q},t)$. It was first proposed to solve the problem of spacecraft and has been widely used until

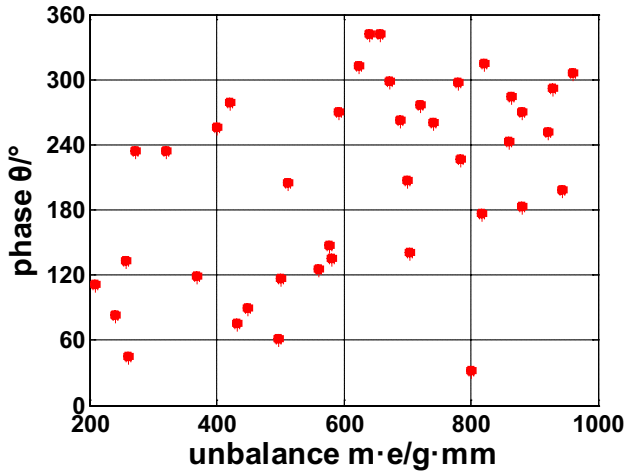

(a) Distribution of unbalance in the LPC

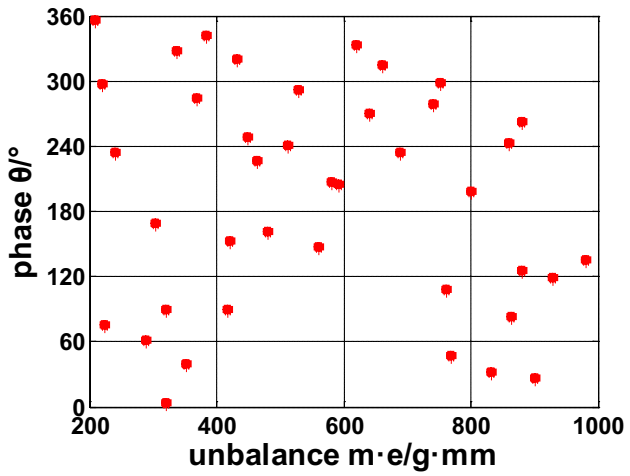

(b) Distribution of unbalance in the HPC

Fig. 5 The distribution of training points

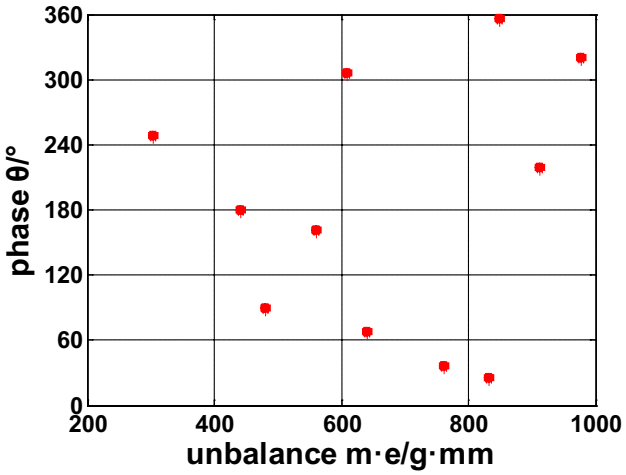

(a) Distribution of unbalance in the LPC

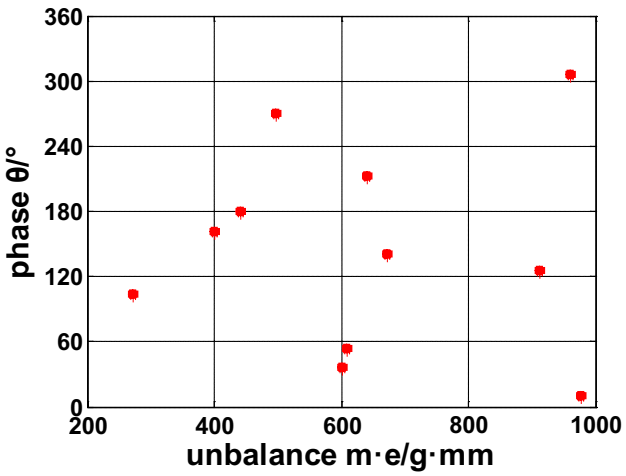

(b) Distribution of unbalance in the HPC

Fig. 6 The distribution of testing points

now. Its advantages are that the number of equations is the least, the number of coordinates of the tree topology system is equal to the degree of freedom of the system, and the dynamics equation is easily converted into ordinary differential equations.

After this process, the time-domain signals are extracted and the response values under the excitation of rotational frequencies N1 and N2, namely the vibration amplitudes, are obtained through the Fast Fourier Transform (FFT), as shown in Fig. 7; N1 (40 Hz) represents the rotational frequency of the LP rotor, and N2 (117 Hz) represents the rotational frequency of the HP rotor; the array, (N1, N2), is the crawling state of the dual-rotor system. From Fig. 7, the law can be seen that unbalance vibration of the dual-rotor system is mainly excited by rotation speeds and it is different from the single rotor that the more complicated structure of the dual-rotor will cause coupled oscillation between LP rotor and HP rotor that amplitudes excited by N1 and N2 are distributed in the whole system. What's more, the unbalance vibration contributions from N1 and N2 vary as there exist different unbalance distributions in LPC and HPC, so this is the core of the work.

The simulation results of training points are shown in Fig. 8. The simulation results of testing points are shown in Table 1. The Pearson correlation coefficient $R^{*,Y}$ for training and test sets can be separately found respectively in Tables 2, 3, 4 and 5, in which Y means output

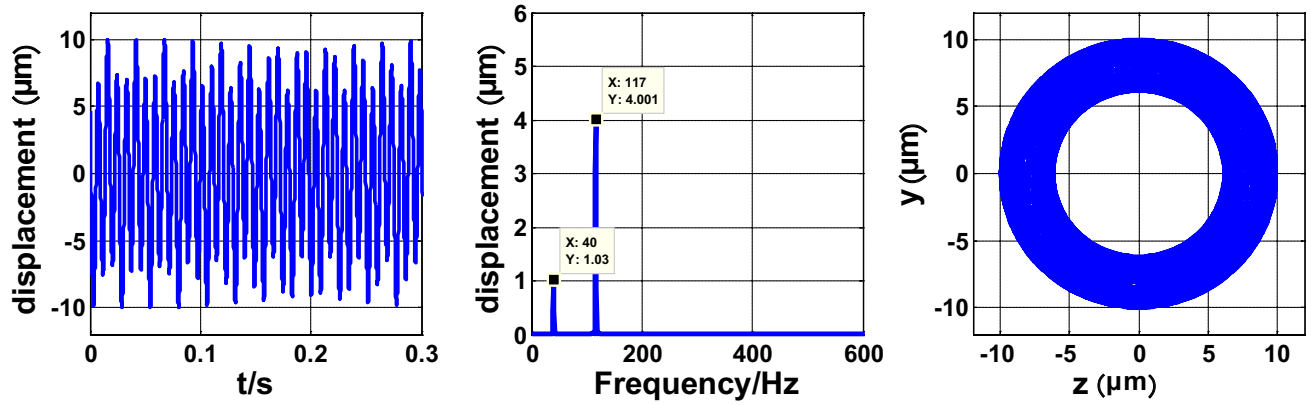

Fig. 7 Time domain graph, spectrum graph and graph of axle center trail at the measuring point 1

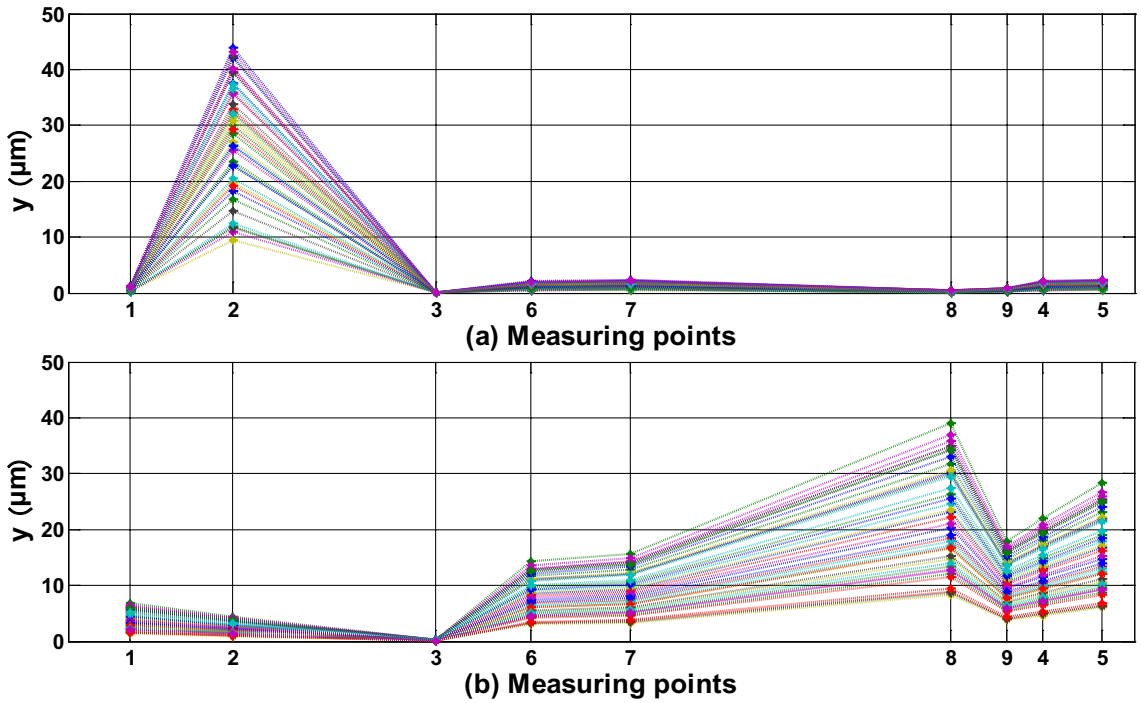

Fig. 8 Amplitudes excited by N1 and N2 based on training points **a** under N1, **b** under N2

Table 1 The partial results based on testing points/μm

Rotate speed	Working condition	Measuring points								
		1	2	3	4	5	6	7	8	9
N1	1	1.04	38.07	0.09	1.80	1.99	0.44	0.76	1.84	2.02
	2	0.80	29.29	0.07	1.38	1.52	0.36	0.59	1.41	1.55
	3	0.76	27.82	0.07	1.31	1.45	0.33	0.56	1.34	1.47
N2	1	3.42	2.23	0.15	7.22	7.95	19.74	9.10	11.15	14.32
	2	4.42	2.87	0.20	9.31	10.25	25.46	11.74	14.38	18.47
	3	6.29	4.10	0.28	13.27	14.60	36.28	16.72	20.49	26.32

Table 2 The Pearson correlation coefficient $R^{*,Y}$ for training sets under N1

$R^{*,Y}$	The position of measuring points								
	1	2	3	4	5	6	7	8	9
$R^{A,Y}$	1.0000	1.0000	1.0000	1.0000	1.0000	0.9963	0.9996	0.9999	0.9999
$R^{B,Y}$	0.4794	0.4800	0.4803	0.4791	0.4788	0.4881	0.4813	0.4791	0.4787
$R^{C,Y}$	0.0177	0.0166	0.0159	0.0181	0.0181	−0.0006	0.0122	0.0192	0.0198
$R^{D,Y}$	−0.0412	−0.0415	−0.0418	−0.0407	−0.0409	−0.0462	−0.0453	−0.0394	−0.0392

Table 3 The Pearson correlation coefficient $R^{*,Y}$ for training sets under N2

$R^{*,Y}$	The position of measuring points								
	1	2	3	4	5	6	7	8	9
$R^{A,Y}$	0.0166	0.0167	0.0163	0.0166	0.0166	0.0166	0.0164	0.0165	0.0165
$R^{B,Y}$	−0.1283	−0.1283	−0.1286	−0.1283	−0.1283	−0.1283	−0.1284	−0.1284	−0.1284
$R^{C,Y}$	1.0000	1.0000	1.0000	1.0000	1.0000	1.0000	1.0000	1.0000	1.0000
$R^{D,Y}$	−0.1631	−0.1631	−0.1631	−0.1631	−0.1630	−0.1631	−0.1630	−0.1632	−0.1632

Table 4 The Pearson correlation coefficient $R^{*,Y}$ for testing sets under N1

$R^{*,Y}$	The position of measuring points								
	1	2	3	4	5	6	7	8	9
$R^{A,Y}$	1.0000	1.0000	1.0000	1.0000	1.0000	0.9935	0.9996	0.9999	0.9999
$R^{B,Y}$	0.1425	0.1408	0.1405	0.1420	0.1420	0.1268	0.1426	0.1398	0.1400
$R^{C,Y}$	0.4180	0.4181	0.4183	0.4173	0.4175	0.4179	0.4172	0.4172	0.4168
$R^{D,Y}$	−0.2616	−0.2584	−0.2568	−0.2620	−0.2620	−0.1981	−0.2460	−0.2648	−0.2661

Table 5 The Pearson correlation coefficient $R^{*,Y}$ for testing sets under N2

$R^{*,Y}$	The position of measuring points								
	1	2	3	4	5	6	7	8	9
$R^{A,Y}$	0.4180	0.4180	0.4180	0.4182	0.4181	0.4181	0.4181	0.4182	0.4180
$R^{B,Y}$	0.4205	0.4206	0.4206	0.4207	0.4204	0.4205	0.4202	0.4209	0.4205
$R^{C,Y}$	1.0000	1.0000	1.0000	1.0000	1.0000	1.0000	1.0000	1.0000	1.0000
$R^{D,Y}$	−0.0256	−0.0257	−0.0257	−0.0259	−0.0257	−0.0257	−0.0256	−0.0259	−0.0257

parameters (amplitudes) and * represents input parameters that A and B are respectively unbalance mass and angle phase of LPC while C and D are respectively unbalance mass and phase angle of HPC. From Tables 2 and 4, it can be seen that the amplitude under N1 is strongly correlated with unbalance mass of LPC, mediumly correlated with unbalance phase angle of LPC while weakly and weakly negatively correlated with unbalance mass and phase angle of HPC respectively; from Tables 3 and 5, it can be seen that the amplitude under N2 is strongly correlated with unbalance mass of HPC, mediumly correlated with unbalance phase angle of HPC while weakly and negatively correlated with unbalance mass and phase angle of LPC respectively.

In this work, the mean square error (MSE) and error rate of the vibration response value are used as the error analysis standards of the surrogate models.

MSE is expressed as,

$$\mathrm{MSE} = \frac{1}{N}\sum_{i=1}^{N}\left(y_i - y_i'\right)^2 \tag{1}$$

where N is the number of testing points, y_i is the simulation result, and y_i' is the corresponding predicted response values. The smaller the value of MSE is, the closer it is to 0, the higher precision of the model.

If $\mu_{simulate}$ and $\mu^*_{predicted}$ respectively represent response value through simulation and prediction of the testing samples excited by the rotate frequency, the expression of error rate, ε^*_μ is defined as,

$$\varepsilon^*_\mu = \frac{\mu_{simulate} - \mu^*_{predicted}}{\mu_{simulate}} \times 100\% \tag{2}$$

Table 6 Predicted amplitudes in N1 of 3 working conditions/μm

Working condition	Surrogate models	Measuring points								
		1	2	3	4	5	6	7	8	9
1	MARS	1.04	38.07	0.09	1.80	1.99	0.47	0.75	1.84	2.03
	RBF	1.02	37.25	0.09	1.76	1.95	0.43	0.74	1.80	1.98
	Kriging	1.04	38.06	0.09	1.79	1.99	0.45	0.76	1.83	2.02
2	MARS	0.80	29.28	0.07	1.38	1.53	0.34	0.58	1.42	1.56
	RBF	0.80	29.17	0.07	1.38	1.52	0.34	0.58	1.41	1.55
	Kriging	0.80	29.28	0.07	1.38	1.53	0.35	0.59	1.41	1.55
3	MARS	0.76	27.82	0.07	1.31	1.45	0.32	0.55	1.35	1.48
	RBF	0.76	27.93	0.07	1.32	1.46	0.33	0.56	1.35	1.49
	Kriging	0.76	27.82	0.07	1.31	1.45	0.32	0.56	1.34	1.48

Table 7 Predicted amplitudes in N2 of 3 working conditions

Working condition	Surrogate models	Measuring points								
		1	2	3	4	5	6	7	8	9
1	MARS	3.42	2.23	0.15	7.22	7.94	19.73	9.10	11.15	14.32
	RBF	3.44	2.24	0.16	7.26	7.99	19.85	9.16	11.22	14.40
	Kriging	3.42	2.23	0.15	7.22	7.94	19.73	9.10	11.15	14.31
2	MARS	4.42	2.87	0.20	9.31	10.25	25.46	11.74	14.38	18.47
	RBF	4.45	2.90	0.20	9.38	10.32	25.65	11.83	14.49	18.61
	Kriging	4.42	2.87	0.20	9.31	10.25	25.46	11.74	14.38	18.47
3	MARS	6.29	4.09	0.28	13.27	14.60	36.28	16.72	20.49	26.32
	RBF	6.23	4.06	0.28	13.15	14.46	35.94	16.57	20.31	26.07
	Kriging	6.29	4.10	0.28	13.27	14.60	36.28	16.73	20.50	26.32

Table 8 Average computing time of the surrogate models

Surrogate models	MARS	RBF	Kriging
Computing time/s	0.01	0.001	0.1

where * refers to the type of the surrogate models, which can be MARS, RBF, and Kriging.

2.3 Algorithms

In this study, the surrogate models of vibration responses at each measuring point are established based on the following three algorithms where linear functions are all important components, all of which are multiple-input and single-output. The input variables are unbalance parameters of the training samples, while the output variables are the corresponding vibration responses. The method of multivariate adaptive regression splines, shorted as MARS, is a form of non-parametric regression analysis to model nonlinearities and interactions between variables [22], and chooses piecewise truncated linear functions to estimate the Eq. (3) expressed by the input variable $\boldsymbol{x}$.

$$y = f(x) + \varepsilon \tag{3}$$

where ε is the predicted error, $x = (x_1, x_2, \cdots, x_p)^T$ is input variables, p is the number of training points, and the column number of matrix $\boldsymbol{x}$ is the number of response variable $\boldsymbol{y}$.

MARS is to form reflected pairs for the each predictor variable, $x_j, j \in \{1, \ldots, p\}$ with corresponding knots at all distinct relating values, $x_{ij}, i \in \{1, \ldots, n\}$, where n is the sample size, expressed by the set C in Eq. (4).

$$C = \left\{ (x_j - t)_+, (t - x_j)_+ \middle| \begin{array}{l} t \in \{x_{1j}, x_{2j}, \cdots, x_{nj}\}, \\ j \in \{1, \cdots, p\} \end{array} \right\} \tag{4}$$

For a given vector of predictor variables $\boldsymbol{x}$ and the target variable $f(x)$, the form of the MARS model approximating the function in Eq. (3) is defined as

$$f(x) = \beta_0 + \sum_{m=1}^{M} \beta_m \cdot B_m(x) \tag{5}$$

where $B_m(x)$ represents a truncated linear function from set C or tensor product of more than one function, and M is the number of truncated linear function in the current model [22, 23]. For multiple variable cases, multiplying an

Table 9 The residual results based on testing points/μm

Rotate speed	Working condition	Measuring points								
		1	2	3	4	5	6	7	8	9
N1	4	0.38	13.91	0.03	0.66	0.73	0.16	0.28	0.67	0.74
	5	1.14	41.72	0.10	1.97	2.18	0.49	0.84	2.01	2.21
	6	0.55	20.14	0.05	0.95	1.06	0.22	0.40	0.98	1.08
	7	1.07	38.80	0.09	1.83	2.03	0.43	0.76	1.88	2.08
	8	0.96	34.78	0.08	1.65	1.82	0.38	0.68	1.69	1.87
	9	0.70	25.63	0.06	1.21	1.34	0.31	0.51	1.23	1.36
	10	1.22	44.65	0.11	2.11	2.33	0.52	0.89	2.15	2.38
	11	0.60	21.97	0.05	1.03	1.14	0.26	0.44	1.06	1.17
N2	4	1.88	1.22	0.08	3.96	4.36	10.83	4.99	6.12	1.88
	5	4.20	2.73	0.19	8.85	9.74	24.19	11.15	13.66	4.20
	6	3.04	1.98	0.14	6.40	7.05	17.50	8.08	9.89	3.04
	7	6.73	4.38	0.30	14.20	15.62	38.80	17.89	21.93	6.73
	8	4.14	2.69	0.19	8.73	9.61	23.87	11.01	13.48	4.14
	9	6.62	4.31	0.30	13.97	15.37	38.19	17.61	21.57	6.62
	10	4.64	3.02	0.21	9.78	10.76	26.74	12.33	15.11	4.64
	11	2.76	1.80	0.12	5.82	6.40	15.91	7.34	8.99	2.76

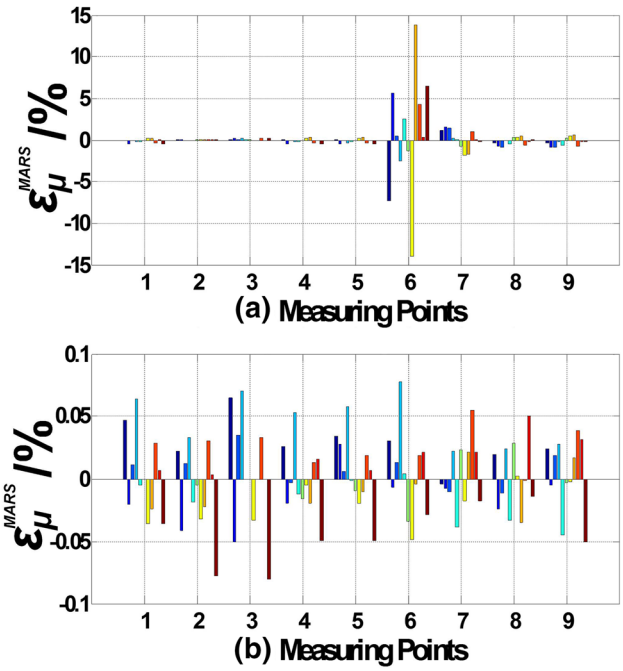

Fig. 9 Error rate histograms of MARS **a** under N1, **b** under N2

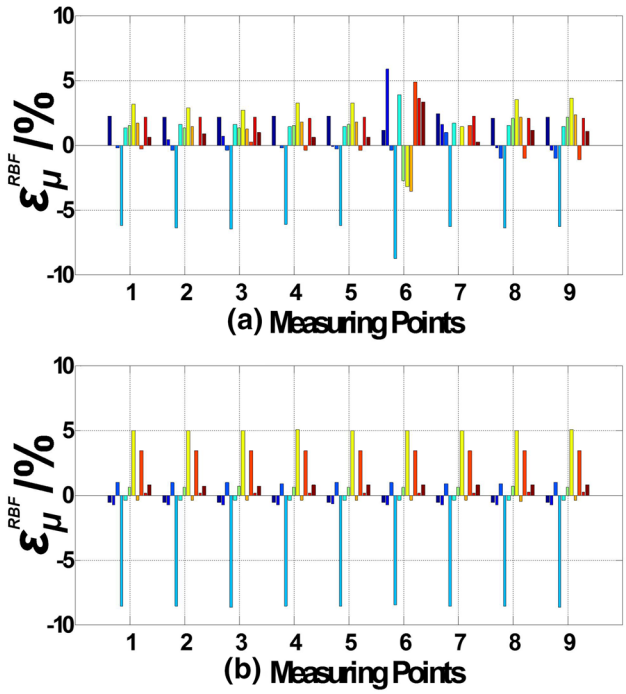

Fig. 10 Error rate histograms of RBF **a** under N1, **b** under N2

existing piecewise linear basis function (BF) with a truncated linear function involving a new variable where both components are nonzero can create the interaction terms which is nonzero only over the space of predictors in MARS [24].

For a real problem, the model building strategy of radial basis function (RBF) is to construct an approximate model by linear superposition of radial basis functions, expressed as Eq. (6) [25],

$$f^{o}(x) = \sum_{k=1}^{M} W_{ik} \cdot \Phi_i\left(\left\|x - c_{ki}\right\|_2\right) \tag{6}$$

where w_{ik} is the synaptic weight between the kth neuron of the output layer of the second hidden layer and the ith

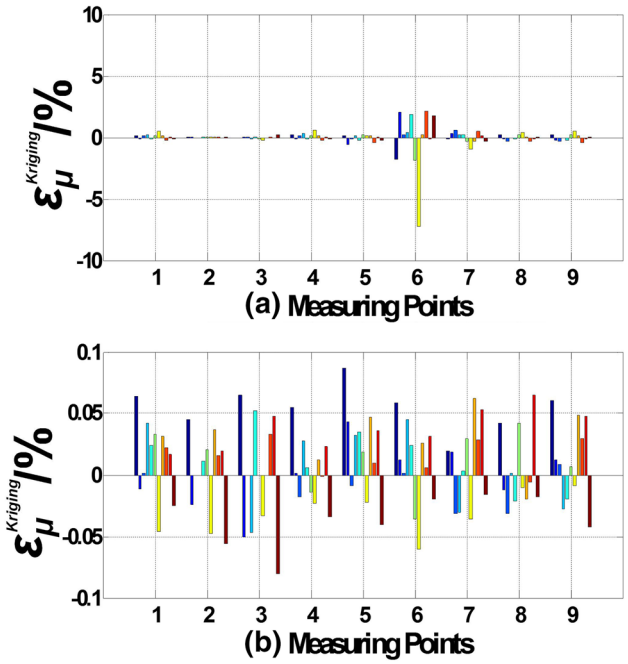

Fig. 11 Error rate histograms of Kriging **a** under N1, **b** under N2

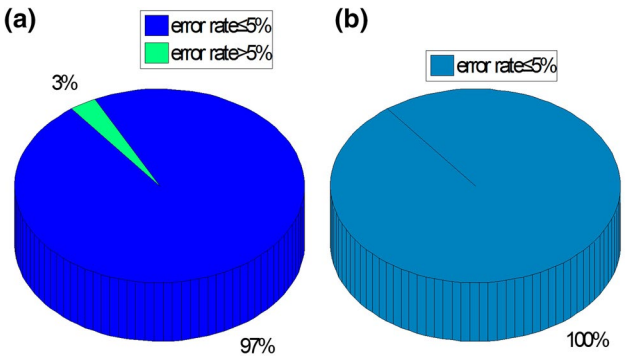

Fig. 12 The pie charts of MARS's error rates **a** under N1, **b** under N2

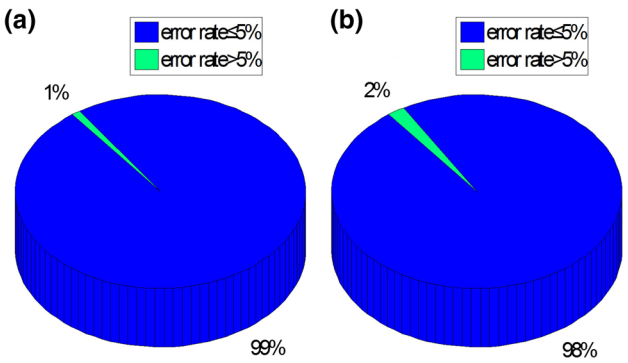

Fig. 13 The pie charts of RBF's error rates **a** under N1, **b** under N2

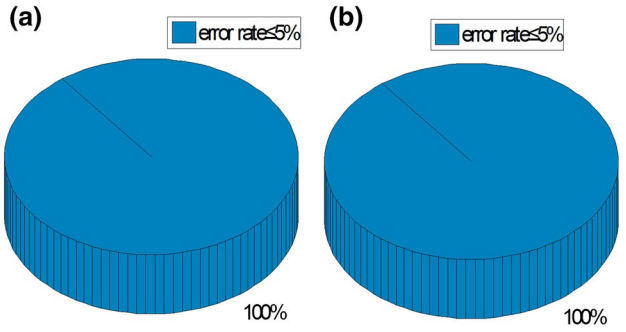

Fig. 14 The pie charts of Kriging's error rates **a** under N1, **b** under N2

neuron of the output layer, c_{ki} is the ith hidden center vector for the kth pattern class of the first hidden layer, $\|\cdot\|_2$ is the Euclidean norm, M denotes the number of neurons in the output layer and the second hidden layer, namely the patterns class number for the training samples set, $\Phi_i(\cdot)$ is the kernel function guaranteeing the required accuracy. In this work, the Multiquadric is the choice, written as Eq. (7) [26],

$$\Phi_i\left(\|x - c_{ki}\|_2\right) = \left(\|x - c_{ki}\|_2^2 + \sigma_i^2\right)^{1/2} \tag{7}$$

where σ_i is the width of the receptive field.

Kriging constructs an unbiased estimation model with the minimum estimation variance characteristics of local estimation. It consists of a linear regression model and an extra random function, which, for the input variable $\boldsymbol{x} = (x_1, \ldots, x_i, \ldots, x_j, \ldots, x_m)^T$, can be defined as Eq. (8) [27],

$$G(x) = \sum_{h=1}^{p} \beta_h \cdot g_h(x) + z(x) = g^T(x)\beta + z(x) \tag{8}$$

The first function of Eq. (9) is a realization of a regression function and $g_h(x)$, $(h = 1, 2, \ldots, p)$ is the basis regression function; the second is a stochastic process (random function) whose mean is 0 and the covariance of random process $z(x)$ is

$$Cov\left[z\left(x_i, x_j\right)\right] = \sigma^2 R\left(c, x_i, x_j\right) \tag{9}$$

where $R(c, x_i, x_j)$ is the correlation coefficient between $z(x_i)$ and $z(x_j)$ with parameter c and σ^2 is the process variance. The correlation function used in this study is the Gaussian, which is expressed as Eq. (10),

$$R\left(c, x_i, x_j\right) = \prod_{n=1}^{N} \exp\left(-c_n\left(x_i^n - x_j^n\right)\right) \tag{10}$$

where x_i^n is the nth component of x_i.

Table 10 Predicted amplitudes in N1 of residual working conditions/μm

Working condition	Surrogate models	Measuring points								
		1	2	3	4	5	6	7	8	9
4	MARS	0.38	13.91	0.03	0.66	0.73	0.16	0.28	0.67	0.74
	RBF	0.41	14.80	0.04	0.70	0.77	0.17	0.30	0.71	0.78
	Kriging	0.38	13.92	0.03	0.65	0.73	0.16	0.28	0.67	0.74
5	MARS	1.14	41.72	0.10	1.97	2.18	0.48	0.84	2.02	2.23
	RBF	1.13	41.08	0.10	1.94	2.14	0.47	0.82	1.98	2.18
	Kriging	1.14	41.72	0.10	1.97	2.18	0.48	0.84	2.01	2.22
6	MARS	0.55	20.14	0.05	0.95	1.06	0.22	0.40	0.97	1.08
	RBF	0.54	19.87	0.05	0.94	1.04	0.23	0.40	0.96	1.06
	Kriging	0.55	20.14	0.05	0.95	1.05	0.23	0.40	0.97	1.08
7	MARS	1.06	38.80	0.09	1.83	2.03	0.49	0.78	1.88	2.07
	RBF	1.03	37.71	0.09	1.78	1.97	0.44	0.75	1.82	2.00
	Kriging	1.06	38.80	0.09	1.82	2.03	0.46	0.77	1.88	2.07
8	MARS	0.95	34.77	0.08	1.64	1.82	0.33	0.70	1.68	1.85
	RBF	0.94	34.28	0.08	1.62	1.79	0.39	0.68	1.65	1.82
	Kriging	0.95	34.76	0.08	1.64	1.82	0.38	0.69	1.69	1.86
9	MARS	0.70	25.62	0.06	1.21	1.34	0.29	0.51	1.24	1.37
	RBF	0.70	25.63	0.06	1.21	1.34	0.29	0.51	1.25	1.37
	Kriging	0.70	25.62	0.06	1.21	1.34	0.30	0.51	1.24	1.36
10	MARS	1.22	44.65	0.11	2.11	2.33	0.52	0.89	2.16	2.38
	RBF	1.20	43.69	0.10	2.06	2.28	0.50	0.87	2.11	2.33
	Kriging	1.22	44.65	0.11	2.11	2.33	0.52	0.89	2.16	2.38
11	MARS	0.60	21.96	0.05	1.04	1.15	0.24	0.44	1.06	1.17
	RBF	0.60	21.78	0.05	1.03	1.14	0.25	0.43	1.05	1.16
	Kriging	0.60	21.96	0.05	1.03	1.15	0.25	0.44	1.06	1.17

Kriging selects the Best Linear Unbiased Predictor (BLUP), which minimizes the Mean Squared Errors (MSE) of the predictor [28],

$$\min_{c} MSE\left[G^{o}\left(x_i\right)\right] = \min_{c}\left[G^{o}\left(x_i\right) - Y\left(x_i\right)\right]. \tag{11}$$

3 Prediction and accuracy tests

The parameters in the training points are used to establish the prediction models and those of testing set are used as input variables to predict the vibration response amplitudes at the measuring points. The specific prediction results of surrogate models are shown in Tables 6 and 7, which are corresponding with the data in Table 1 from the first three working conditions of the testing set. The experimental results and prediction results of the other 8 working conditions are shown in Tables 9, 10, 11. It can be seen that the prediction results converge to the simulation results by comparison.

Table 8 shows the average calculation time of each algorithm when predicting. As can be seen from it, the computing efficiencies are all very high; the most efficient is RBF, followed by MARS and Kriging.

In fact, ADAMS simulation can also be used to predict the vibration response, showed as Tables 1 and 9. However, compared with metamodelling methods, it has three disadvantages. Firstly, ADAMS' calculation time is about 10 s in this paper, which has a lower prediction efficiency according to Table 8 when ran in the same computer; secondly, complex multi-body dynamics simulation procedures, including the establishment of 3D model, settings of constraint conditions and driving motions, etc. all consume much time, which can be saved by metamodelling methods; thirdly, compared with surrogate model algorithm, multi-body dynamics methods require a higher computer configuration, especially CPU and RAM. So we choose the surrogate models to predict vibration response in rotor dynamics instead of the dynamics simulation.

Based on the simulation values and the predicted values of the surrogate models in testing points, the error rate histograms at the 9 measurement points under N1 and N2 are obtained, as shown in Figs. 9, 10 and 11. Figure 9 shows that MARS's error rates under N1 are mostly less than 5%, and those under N2 are all ranging from −0.1 to −0.1%,

Table 11 Predicted amplitudes in N2 of residual working conditions/μm

Working condition	Surrogate models	Measuring points								
		1	2	3	4	5	6	7	8	9
4	MARS	1.88	1.22	0.08	3.96	4.36	10.82	4.99	6.11	7.85
	RBF	2.04	1.33	0.09	4.30	4.73	11.76	5.42	6.64	8.53
	Kriging	1.88	1.22	0.09	3.96	4.36	10.83	4.99	6.11	7.86
5	MARS	4.20	2.73	0.19	8.85	9.74	24.19	11.15	13.66	17.55
	RBF	4.21	2.74	0.19	8.88	9.77	24.28	11.19	13.72	17.61
	Kriging	4.19	2.73	0.19	8.85	9.73	24.18	11.15	13.66	17.54
6	MARS	3.04	1.98	0.14	6.40	7.05	17.51	8.07	9.89	12.70
	RBF	3.02	1.96	0.14	6.37	7.00	17.40	8.02	9.83	12.62
	Kriging	3.04	1.98	0.14	6.40	7.04	17.51	8.07	9.89	12.70
7	MARS	6.73	4.38	0.30	14.20	15.62	38.82	17.89	21.93	28.16
	RBF	6.39	4.16	0.29	13.49	14.84	36.87	17.00	20.83	26.75
	Kriging	6.73	4.38	0.30	14.20	15.62	38.82	17.90	21.93	28.16
8	MARS	4.14	2.69	0.19	8.73	9.61	23.87	11.01	13.48	17.32
	RBF	4.16	2.71	0.19	8.77	9.65	23.97	11.05	13.54	17.39
	Kriging	4.14	2.69	0.19	8.73	9.60	23.86	11.00	13.48	17.31
9	MARS	6.62	4.31	0.30	13.97	15.37	38.18	17.60	21.57	27.70
	RBF	6.40	4.16	0.29	13.50	14.85	36.89	17.01	20.84	26.76
	Kriging	6.62	4.31	0.30	13.97	15.37	38.19	17.61	21.57	27.70
10	MARS	4.64	3.02	0.21	9.78	10.76	26.73	12.33	15.10	19.39
	RBF	4.63	3.01	0.21	9.77	10.75	26.70	12.31	15.08	19.36
	Kriging	4.64	3.02	0.21	9.78	10.76	26.73	12.32	15.10	19.39
11	MARS	2.76	1.80	0.12	5.82	6.41	15.91	7.34	8.99	11.55
	RBF	2.74	1.78	0.12	5.78	6.35	15.79	7.28	8.92	11.45
	Kriging	2.76	1.80	0.12	5.82	6.40	15.91	7.34	8.99	11.54

with a better accuracy. Figure 10 shows that RBF's error rates under N1 and N2 are all mostly less than 10%, except testing point 4, whose predicted values are obviously bigger than the corresponding simulated at all measurement points for the error rates ranging from − 10 to − 5%, no matter what in N1 or N2, according the Eq. (2) above. Figure 11 shows that Kriging's error rates are ranging from − 0.1 to 0.1% in N2, while − 0.92% to 0.6% in N1 except those at measuring point 6 ranging from − 7.22 to − 2.15%.

If the maximum error rate 5% is taken as a standard to evaluate the predicted accuracy, the pie charts of the error rates are drawn in Figs. 12, 13 and 14. In these three figures, the Kriging's ratios are all 100%, the RBF's ratios are 99% and 98% respectively, and the MARS's ratios are 97% and 100% respectively, under N1 and N2 (Tables 10, 11).

The comparison of MSE values based on testing points from MARS, RBF and Kriging can be seen in Figs. 15 and 16, where Logarithmic Coordinates are used. The larger the MSE values, the smaller the ordinates.

From Fig. 15, the MSE values of the RBF model at measuring point 2 of the LP rotor are much higher than those of MARS and Kriging under N1, so the prediction accuracy of the RBF model here is much lower; at the other measuring points of the LP rotor, MSE values of all models are less than 5e-02, with high prediction accuracy. At the measuring points of the HP rotor, MSE values of all models are less than 3e-02, so the prediction accuracy is also quite high. In general, the magnitude order from the models at measurement points of the HP section is: RBF > MARS > Kriging, so the order of precision is: Kriging > MARS > RBF.

It can be seen from Fig. 16 that, at all measuring points under N2, the MSE values of MARS and Kriging are much smaller than those of RBF, with higher prediction accuracies.

4 Conclusions

In this work, based on the research finding that the vibration of dual-rotor system is caused by the coupled excitations of rotational frequencies N1 and N2, three kinds of surrogate models, MARS, RBF and Kriging, are established under finite working conditions to predict unknown unbalance responses of a simplified dual-rotor model of aero-engine. And it is proved that the predicted results

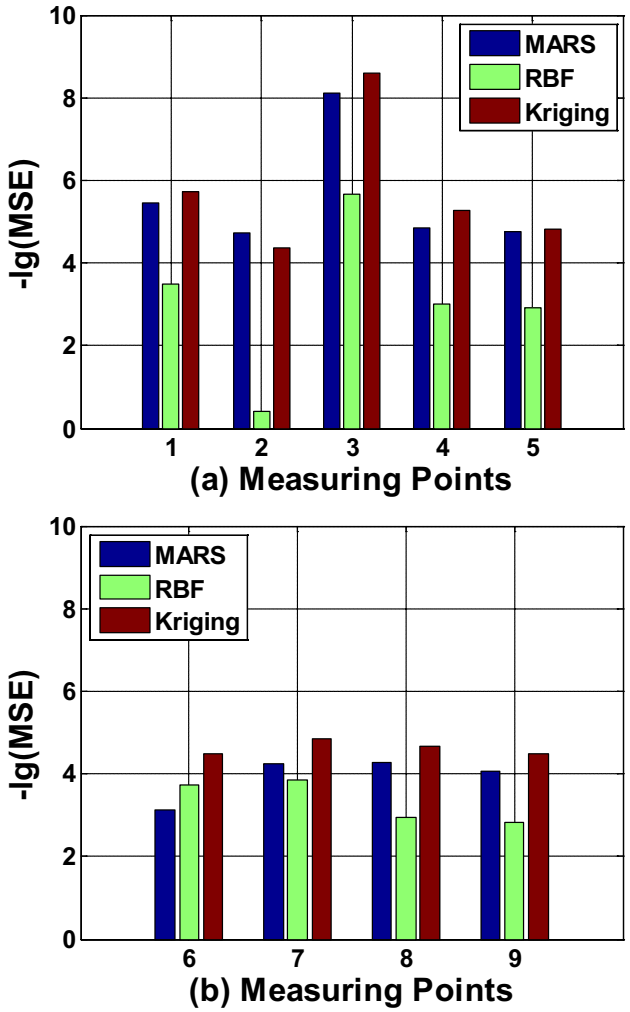

Fig. 15 Comparison of MSE values of the models at the measuring points under N1 **a** in LP rotor, **b** in HP rotor

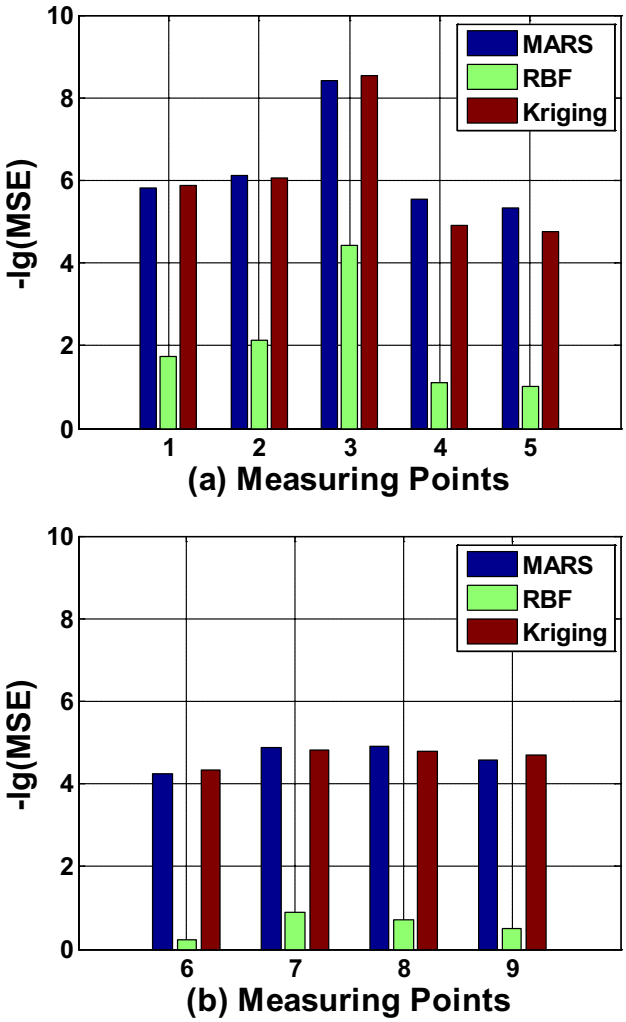

Fig. 16 Comparison of MSE values of the models at the measuring points under N2 **a** in LP rotor, **b** in HP rotor

have high accuracies, according to analyzation and comparison with the selected standards.

1. The predicted unbalance response values of these three algorithms basically converge to the corresponding simulation results under N1 and N2;
2. The three algorithms are high-efficiency, among which RBF is the fastest, while Kriging is the slowest by contrast.
3. Compared with those under N2, the error rates under N1 are significantly bigger, so the precision order is the opposite. The reason of the phenomenon is that the vibration amplitudes under N1 are significantly smaller than those under N2, so the former is more difficult to accurately predict.
4. When the maximum error rate of 5% is taken as an evaluation standard, the predicted results of Kriging's are the most precise, and under N1 and N2 the MARS and the RBF respectively have better performances by contrast.
5. The MSE of testing points taken as an evaluation standard, the three surrogate models all have high prediction accuracies; the MSE values of RBF are obviously larger than those of the others, which accuracy is the lowest by contrast. Under N1, the Kriging's accuracy is a little better than that of the MARS, but under N2, the two are much the same.

Acknowledgments This work was supported by National Natural Science Foundation of China (Grant No. 51705064).

Compliance with ethical standards

Conflict of interest The authors declare that they have no conflict of interest.

References

1. AL-Shudeifat MA, Al Hosani H, Saeed AS, Balawi S (2019) Effect of unbalance force vector orientation on the whirl response of cracked rotors. J Vib Acoust 141(2):021001. https://doi.org/10.1115/1.4041462
2. Gao P, Hou L, Yang R, Chen Y (2019) Local defect modelling and nonlinear dynamic analysis for the inter-shaft bearing in a dual-rotor system. Appl Math Model 68:29–47
3. Cao H, He D, Xi S, Chen X (2018) Vibration signal correction of unbalanced rotor due to angular speed fluctuation. Mech Syst Signal Process 107:202–220
4. Yang W, Liang M, Wang L, Yuan H (2018) Research on unbalance response characteristics of gas turbine blade-disk rotor system. J VibroEng 20(4):1676–1690
5. Zhang ZX, Wang LZ, Jin ZJ, Zhang Q, Li XL (2013) Non-whole beat correlation method for the identification of an unbalance response of a dual-rotor system with a slight rotating speed difference. Mech Syst Signal Process 39(1–2):452–460
6. Blanning RW (1975) The construction and implementation of metamodels. Simulation 24(6):177–184. https://doi.org/10.1177/003754977502400606
7. Motosh N (1976) Determination of joint stiffness in bolted connections. J Eng Ind 98(3):858–861
8. Sacks J, Welch WJ, Mitchell TJ, Wynn HP (1989) Design and analysis of computer experiments. Stat Sci 4:409–423
9. Simpson TW, Poplinski JD, Koch PN, Allen JK (2001) Metamodels for computer-based engineering design: survey and recommendations. Eng Comput 17(2):129–150
10. Li W, Padula S (2005) Approximation methods for conceptual design of complex systems. In: Chui C, Neaumtu M, Schumaker L (eds) Approximation theory XI: Gatlinburg 2004. Nashboro Press, Brentwood, pp 241–278
11. Li M, Sadoughi M, Hu C, Hu Z, Eshghi AT, Lee S (2019) High-dimensional reliability-based design optimization involving highly nonlinear constraints and computationally expensive simulations. J Mech Des 141(5):051402
12. Raponi E, Bujny M, Olhofer M, Aulig N, Boria S, Duddeck F (2019) Kriging-assisted topology optimization of crash structures. Comput Methods Appl Mech Eng 348:730–752
13. Hou Y, Zhao Q, Sapanathan T, Dumon A, Rachik M (2019) Parameter identifiability of ductile fracture criterion for DP steels using bi-level reduced surrogate model. Eng Fail Anal 100:300–311
14. Ovissipour M, Rai R, Nitin N (2019) DNA-based surrogate indicator for sanitation verification and predict inactivation of Escherichia coli O157: H7 using vibrational spectroscopy (FTIR). Food Control 100:67–77
15. Sangireddy SAR, Bhatia A, Garg V (2019) Development of a surrogate model by extracting top characteristic feature vectors for building energy prediction. J Build Eng 23:38–52
16. Sinou JJ, Nechak L, Besset S (2018) Kriging metamodeling in rotordynamics: application for predicting critical speeds and vibrations of a flexible rotor. Complexity
17. Fu C, Ren X, Yang Y, Lu K, Qin W (2019) Steady-state response analysis of cracked rotors with uncertain-but-bounded parameters using a polynomial surrogate method. Commun Nonlinear Sci Numer Simul 68:240–256
18. Yujiong Gu, Chen Dongchao, Jing Xu, He Chengbing (2015) Quantitative identification of unbalance in a rotor system based on surrogate model. J Chin Soc Power Eng 35(12):982–987. https://doi.org/10.3969/j.issn.1674-7607.2015.12.006
19. Han F, Guo X, Mo C, Gao H, Hou P (2017) Parameter identification of nonlinear rotor-bearing system based on improved kriging surrogate model. J Vib Control 23(5):794–807
20. Shelke D, Sakurada K (2016) Simulation of gear microgeometry for gear whine noise reduction in passenger car. In Simulation and testing for vehicle technology. Springer, Cham, pp 137–146. https://doi.org/10.1007/978-3-319-32345-9_11
21. Zhang Wei, Song Xueguan, Shi Maolin, Huo J (2019) The lightweight design of the boom of mechanical excavator based on surrogate model technology machinery. J Des Manuf 4:1–4. https://doi.org/10.19356/j.cnki.1001-3997.2019.04.001
22. Friedman JH (1991) Multivariate adaptive regression splines. Ann Stat 19(1):1–67
23. Friedman JH, Silverman BW (1989) Flexible parsimonious smoothing and additive modeling. Technometrics 31(1):3–21
24. Koc EK, Bozdogan H (2015) Model selection in multivariate adaptive regression splines (MARS) using information complexity as the fitness function. Mach Learn 101(1–3):35–58
25. Shen W, Guo X, Wu C, Wu D (2011) Forecasting stock indices using radial basis function neural networks optimized by artificial fish swarm algorithm. Knowl-Based Syst 24(3):378–385
26. Seydaoğlu M (2019) A meshless method for burgers' equation using multiquadric radial basis functions with a Lie-group integrator. Mathematics 7(2):113
27. Sun Z, Wang J, Li R, Tong C (2017) LIF: a new Kriging based learning function and its application to structural reliability analysis. Reliab Eng Syst Saf 157:152–165
28. Kleijnen JP (2009) Kriging metamodeling in simulation: a review. Eur J Oper Res 192(3):707–716

Publisher's Note Springer Nature remains neutral with regard to jurisdictional claims in published maps and institutional affiliations.